Finite element optimization of sample geometry for measuring the torsional shear strength of glass/metal joints

M. Fakouri Hasanabadi [a,*], J. Malzbender [b], S. M. Groß-Barsnick [c], H. Abdoli [d], A. H. Kokabi [a], M. A. Faghihi-Sani [a]

[a] Department of Materials Science and Engineering, Sharif University of Technology, Azadi Avenue, P. O. Box 11155-9466, Tehran, Iran

[b] Forschungszentrum Jülich GmbH, Institute of Energy and Climate Research, IEK-2, 52425 Jülich, Germany

[c] Forschungszentrum Jülich GmbH, Central Institute of Engineering, Electronics and Analytic, ZEA-1, 52425 Jülich, Germany

[d] Department of Renewable Energy, Niroo Research Institute (NRI), P.O. Box 1466551 Tehran, Iran

E-mail addresses: hasanabadi68@gmail.com (M. Fakouri Hasanabadi), j.malzbender@fz-juelich.de (J. Malzbender), s.m.gross@fz-juelich.de (S. M. Groß-Barsnick), hamidabdoli@yahoo.com (H. Abdoli), kokabi@sharif.edu (A. H. Kokabi), faghihi@sharif.edu (M. A. Faghihi-Sani)

Abstract

Assessment of mechanical properties of glass/metal joints is a challenging process, especially when the application relevant conditions of the joints have to be considered in the test design. In this study, a finite element method (FEM) is implemented to analyze a torsional shear strength test designed for glass-ceramic/steel joints aiming towards solid oxide fuel/electrolysis

application. Deviations from axial symmetry of the square flanges (ends) of respective hourglass-shaped specimens and also supporting and loading sockets of the test set-up are included in the model to simulate conditions close to reality. Undesirable tensile stress and also shear stress concentration appear at the outer edge of glass-ceramic layers, which are less for the hollow-full specimen. The simulation results show that for a specimen with 9 mm thick square- and 6 mm thick triangular-flanges, locally enhanced tensile stresses almost disappear, resulting in a symmetric shear stress distribution. The difference between the analytically derived nominal shear strength and the real critical shear stress derived via simulation reduces with decreasing the fracture torque.

Keywords: Torsion test; Finite element simulation; Solid oxide cells; Sealant; Stress; Optimization

1. Introduction

Glasses/glass-ceramics have a different nature of the atomic bonds than metals, which makes it difficult to join both and also to evaluate their mechanical properties in a joined situation [1]. In the past three decades, sealing of planar fuel/electrolysis cell (SOFC/SOEC) stacks has been one of the most challenging applications regarding glass-metal joints [2,3]. In this application, glass/glass-ceramic sealants must join ceramic cells and metallic interconnects/frames in the SOFC/SOEC stack and maintain the gas-tightness often for more than 40,000 h at operation relevant high-temperatures (650–850 °C) as well as during heating and cooling cycles [4,5].

Thermal and chemical strains arise during thermal cycling or steady-state operation of stacks leading to stress generation in the components [6–9]. Therefore, an assessment of stack components regarding their mechanical behavior, in particular for the sealant, is necessary [10]. Extensive experimental work has been conducted to evaluate the fracture toughness [11–13], fracture strength [14–16] and creep behavior [17,18] of glass-ceramic sealants in a joined state, where respective results are especially useful for qualitatively comparison of mechanical behaviors. However, the measured mechanical properties in different laboratories using in particular due to different assessment methods cannot be easily compared, raising questions regarding a standardized tests. Nowadays, finite element simulation is regarded as an efficient tool to assess the effect of test procedure parameters and hence, to subsequently eliminate any systematic errors and bias in the test results [19].

Shear strength is a critical property for the structural integrity of sealing materials in the joint [20]. Although some efforts have been made to evaluate the critical shear stress for failure of glass-ceramic sealants [21–24], the implemented methods were always associated with challenges related to the difficulty to align specimens in the test fixture, localized stress concentrations and unfavorable bending or normal stress (σ) components generated in the specimen [25,26]. However, the torsion test performing on hourglass-shaped specimens appears to be a convenient and promising method to overcome these challenges [27], and for this reason, it attracted increasing interest in the last decade [28–31]. In this method, the square-shaped ends (flanges) of the specimen are slotted into respective supporting and loading sockets, without any need for additional clamping or adhesive. The sealant layer, which joins two steel halves, may be in annulus or disk shape. The nominal shear strength ($\tau_{nominal}$) is usually calculated using following equation [20]:

$$\tau_{nominal} = \frac{2\,T_f\,R_o}{\pi\,(R_o^4 - R_i^4)} \qquad (1)$$

where T_f is the fracture torque, and R_o and R_i are outer and inner radii of the sealant layer, respectively.

Recently, the authors [20] carried out torsion tests on three configurations of hourglass-shaped specimens; so-called full-full (with full halves) with disk-shape sealant, hollow-full (consisting both hollow and full halves) and hollow-hollow (with hollow halves) both with annulus-shaped sealant. The results revealed that there is a dependency of measured nominal shear strength ($\tau_{nominal}$) on specimen's configuration, for which the results of recent finite element analyses [32–34] could not present a reasonable explanation. Indeed, the simulations were done using axisymmetric models assuming that deviation from axial symmetry in the square flanges does not affect the central portion of specimen [32–34]. Also, it was recently observed that, contrary to flexural strength, the shear strength of steel/sealant joint decreases with increasing temperature [16,20]. Any effect of systematic error that might be related to the test itself in this reduction trend of the torsional shear strength with temperature has not been specified yet.

Hence, in the current paper, the stress distribution in the specimen is investigated considering effects of the axial asymmetry of flanges and sockets at two temperatures. In the following, some dimensional changes and also new shapes for flanges are proposed and investigated to improve and ultimately attain an axial symmetric pure shear stress distribution in the joining area.

2. Finite element analyses (FEA)

The simulation was carried out on the basis of three-dimensional (3D) models using finite element software (ANSYS Workbench 16). Fig. 1 shows an example of considered models, in which a specimen with 3 mm thick square flanges is slotted into the sockets. The outer radius and height of sockets are 30-35 mm and 12 mm, respectively. There is a 100 µm gap between the

inner walls of sockets and the outer walls of flanges. More details about the geometry of specimens are given in Ref. [20].

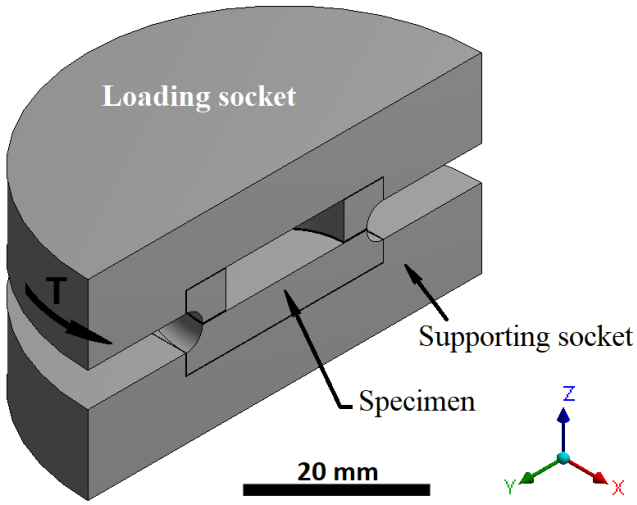

Fig. 1. Schematic drawing of cross-section of square 3 hollow-3 full specimen in the sockets.

The specimen consists of a glass-ceramic layer (sealant H-F) and two halves of Crofer22APU, which are presumed to be in frictionless contact with the Inconel X-750 sockets. Sealant H-F is a composite material containing 13 wt% yttrium stabilized zirconium oxide (YSZ) fiber in a glass matrix of BaO-CaO-SiO_2 ternary system. The glass transition temperature (T_g) and the joining temperature of this sealant are 621 ºC and 850 ºC, respectively [35,36]. Details on the preparation of sealant H-F and joining procedure can be found in Refs. [20,37]. The elastic-plastic behaviors of Crofer22APU and Inconel X-750 are taken into account, but it is assumed that the sealant behaves elastic at both room temperature and 600 ºC. The properties of the materials can be found in Refs. [38–41].

Figure 2 shows schematics of the different types of specimens selected for simulation and respective discussion in the current work. Finite element simulation results of other specimens have been excluded from this paper for brevity. The digits in the name of each specimen refer to

thickness of the flanges. The first three specimens with 3 mm thick square flanges are configurations which have already been used in experimental characterizations [20]. Adapted from ASTM F734 [42] an increase in flange thickness to 9 mm is proposed. The triangular- and hexagonal-flanges have been inspired by bolts. It is worth mentioning that Jung et al. have already used such a hexagonal design for mechanical evaluation of SiC/SiC joints [43].

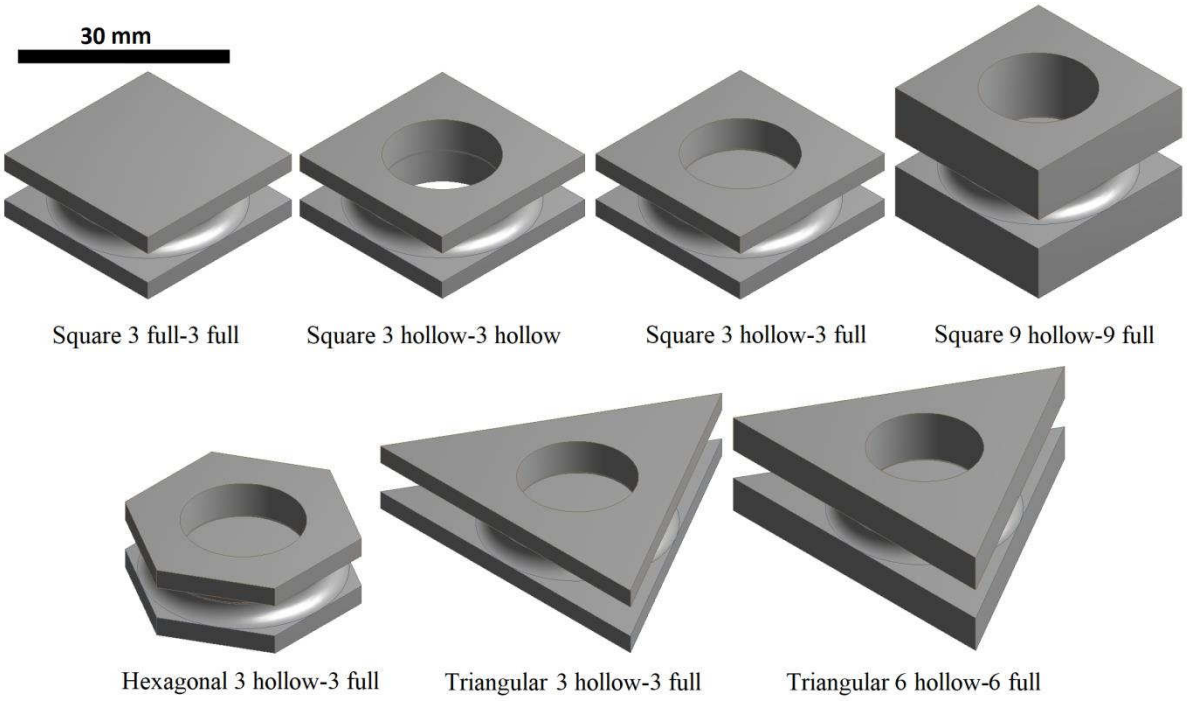

Fig. 2. Schematics of different types of specimens.

The specimens and in particular the sealants have already shown in experiments brittle fracture under a $\tau_{nominal}$ of ~ 60 MPa and ~ 40 MPa at room temperature and 600 ºC, respectively [20]. At each temperature, a torque value corresponding to the $\tau_{nominal}$ (Eq. 1) was applied to the outer wall of loading socket, whereas the outer wall of supporting socket was fixed. In order to simulate the stress distribution in the mid-thickness plane of the sealant, the mesh was optimized by reducing the element size to 5×10^{-2} mm within the sealant area. In addition to the shear

stress (τ), any potential normal stress along the specimen axis (σ_z) was investigated. Also, the first principal stress (σ_1) was obtained for the points on the mid-thickness plane of sealant. The first principal stress (σ_1) is the algebraic maximum normal stress component on the planes on which the shear stress (τ) is zero. Because of rotational symmetry of square and triangular/hexagonal flanges, the analyses' were done on respectively one-quarter and one-third sections of respective models.

4. Results and discussion

Figure 3 illustrates stress distributions in the mid-thickness plane of the sealant for different configurations. As already revealed on the basis of a symmetric model [33,34], the true shear stress at the outer edge of sealant is higher than that calculated by Eq. 1 ($\tau_{nominal}$ = 60 MPa). However, the present asymmetric model verifies that the square flanges of specimens are the origin of the axial asymmetry in the shear stress distribution. Furthermore, some localized tensile stress (σ_z) can be observed at the outer edge of sealant for all configurations. In addition, some minor plastic strains ($< 10^{-4}$ mm·mm^{-1}) appeared in the steel halves within the regions of stress concentration near the sealant/steel interfaces. These plastic strains reach up to 10^{-2} mm·mm^{-1} at the corners of flanges.

Furthermore, it can be seen in Fig. 3 that the shear stresses in hollow-hollow configuration possess the strongest deviation from the axial symmetric distribution, and a considerable area of the sealant is exposed to rather high tensile stresses. This explains why in our previous report the measured nominal shear stress at failure $\tau_{nominal}$ (calculated using the analytical relationship) of 3 hollow-3 hollow specimens (49.1 ± 3.8 MPa [20]) was lower than of both 3 full-3 full and 3 hollow-3 full specimens (57.0 ± 0.4 MPa and 60.3 ± 2.3 MPa, respectively [20]).

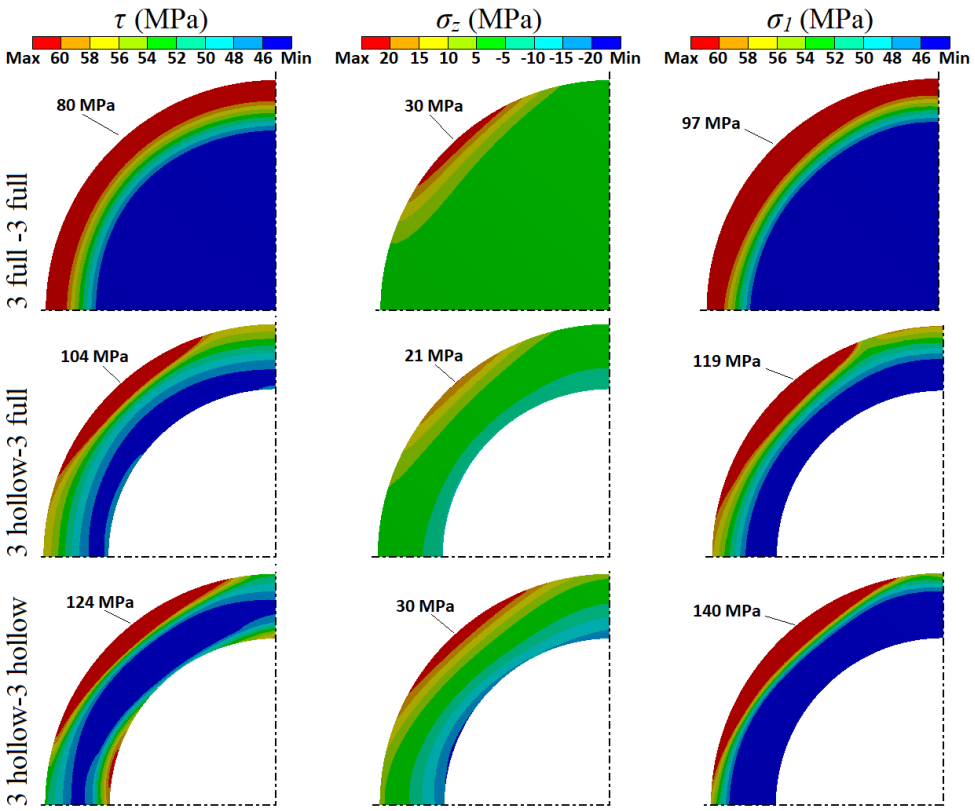

Fig. 3. Effect of configuration of specimens with 3 mm thick square flanges on τ, σ_z and σ_1 distributions in the mid-thickness plane of sealant at room temperature. The maximum stresses are indicated along with their location. The applied torque corresponds to a nominal shear stress $\tau_{nominal}$ of 60 MPa, which calculated using the analytical relationship.

Recent fractographic investigations of failed torsion test specimens [20] revealed that the crack passes through both upper and lower interfaces and creates some strips and traces on the bare surfaces of steel and sealant, respectively. This evidence [20] implies that a number of cracks initiate simultaneously at the triple-phase boundaries steel/sealant/atmosphere and then they grow along the radius and also toward the opposite steel/sealant interface as schematically illustrated in Fig. 4a. But the steel restrains further crack opening, and consequently the mode I stress intensity factor doesn't increase with increasing the crack length. Also, the mixed-mode

stress intensity factor is still not high enough so that the cracks kink to the interface. Therefore, the cracks propagate stably along the surfaces at an angle θ with respect to the z axis. With increasing torque one of the cracks reaches the critical stress intensity for propagation along the interfaces and leads then to catastrophic failure (Fig. 4b).

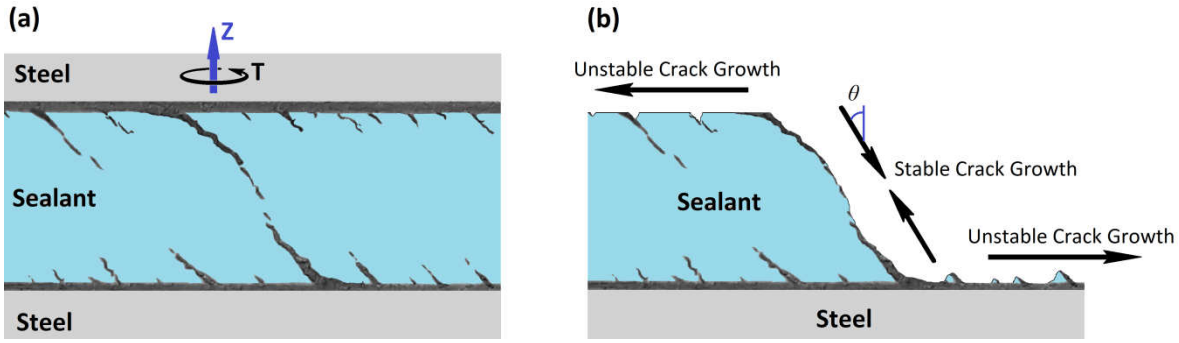

Fig. 4. Schematics of a) cracks which propagate stably in sealant before catastrophic fracture and b) traces of serrated crack path along the sealant/steel interface during unstable crack growth.

During torsion tests, the brittle materials tend to break along planes perpendicular to the direction in which tension possesses its maximum value, i.e., along fracture surfaces at an angle of ~ 45° to the z axis [20]. It is worth noting that this angle can be affected by the elastic moduli mismatch of sealant and steel [44].

As can be seen in Fig. 3, the maximum value of the first principal stress (σ_1) for a hollow-full specimen is higher than for a full-full one, and for this reason, it can be expected that the sealant fails in this case at a lower applied torque. However, the experimental results [20] showed that the $\tau_{nominal}$ of hollow-full specimens is even higher than that of the full-full ones. Although these high values of σ_1 might lead to crack initiation and growth in a direction other than normal to specimens' axis, the steel can restrain further crack opening and finally stop crack growth. The normal stresses along the specimens' axis (σ_z) increase the stable crack growth angle with respect to the z axis (θ in Fig. 4a), and consequently reduce the effect of the steel restrain on

crack growth. Also, σ_z is essential stress for crack growth along the interfaces. Therefore, the magnitude of σ_z is more crucial than that of σ_1 regarding crack growth. This might be the cause of the observed higher $\tau_{nominal}$ of hollow-full specimens compared to that of the full-full ones.

The failure probability of the glass-ceramic sealant, being a brittle material even at 600°C, depends strongly on the existence of discontinuities. Pre-existing pores and/or micro-cracks within the region of stress concentration may lead to sealant fracture at lower torques. On the other hand, it should be recognized that brittle materials are typically weaker in tension than shear [45]. Therefore, both shear stress concentration and localized tensile stress generation increase the sensitivity to existing defects and consequently can enhance the scatter in test results.

Figure 3 shows that the stress distribution in the sealant is more non-uniform for hollow-full and hollow-hollow specimens than for full-full specimens. It was recently observed that perforation of either one half or both steel halves (i.e. using hollow-full and hollow-hollow specimens, respectively) leads to enhanced uncertainty of the results in terms of the standard deviation of $\tau_{nominal}$ [20], which is in agreement with the conclusions derived on the basis of the current simulation results.

As can be seen in Fig. 3, the sealant in hollow-full configuration is exposed to the lowest tensile stress. In fact, the annulus shape of sealant in the hollow-full specimen decreases the required torque for fracture (compared with full-full specimen), and the full half decreases the impact of the square geometry of specimen's flange (compared with the hollow-hollow specimen). However, considering the reported flexural strength of this joint at room temperature (23 ± 1 MPa [46]), the generated tensile stress of 21 MPa appears to be still significant.

To achieve a pure shear loading in the joining area, two other flange shapes were investigated for the hollow-full configuration. Figure 5 reveals that triangular flanges decrease

the shear stress concentrations and also σ_z at the outer edge of sealant, while hexagonal flanges have an opposite effect.

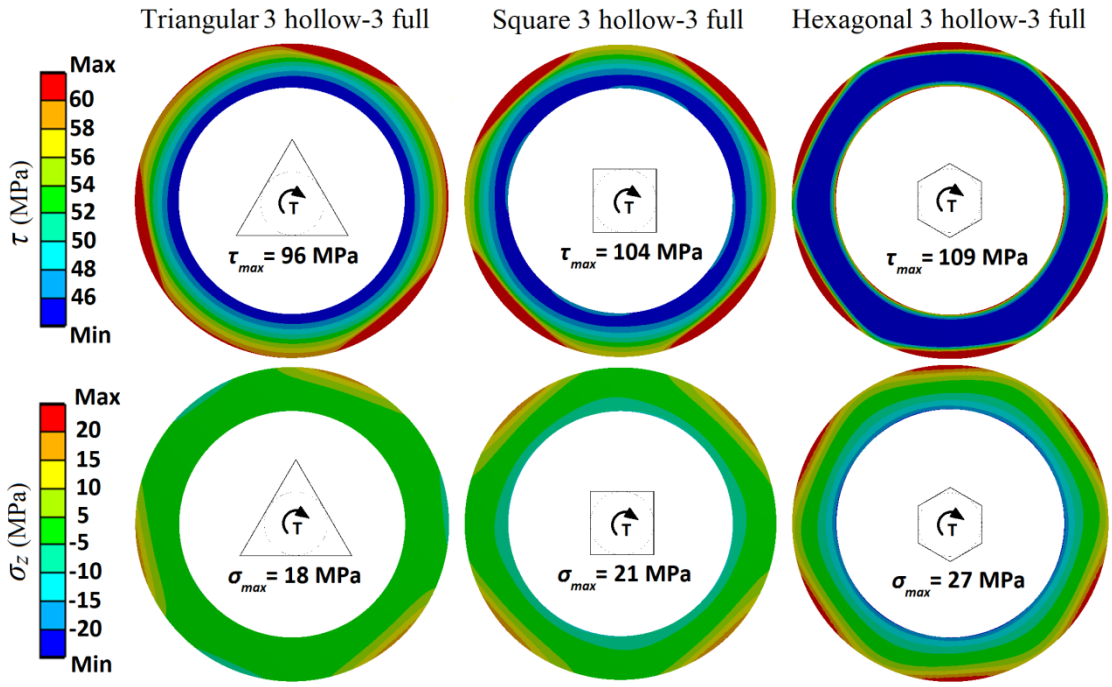

Fig. 5. Distribution of τ and σ_z in the mid-thickness plane of sealant in specimens with 3 mm thick triangular-, square- and hexagonal-flanges at room temperature. The applied torque corresponds to a nominal shear stress $\tau_{nominal}$ of 60 MPa, which calculated using the analytical relationship.

The tensile and compressive stresses at the respective outer and inner edges of the sealant (Fig. 3) are a result of the considerable elastic deformation of the hollow steel halves. Therefore, it seems reasonable that strengthening the flanges can homogenize the stress distribution in the sealant.

It is worth noting that the full-full configuration must tolerate a 37% higher torque than the other configurations (Eq. 1) to reach the same apparent shear strength of the sealant and hence it

can be stated that one of the causes of the high tensile stress generation for this configuration (Fig. 3) is the higher applied torque h_f (Eq. 1) to reach fracture.

As an alternative to the full half, the hollow half might be strengthened by thickening its flanges. In fact, as can be seen in Fig. 6, an increase in thickness of triangular flanges to 6 mm decreases the σ_z down to 4 MPa and also results in an axial symmetric τ and σ_1 distributions in the sealant. A decrease in the maximum σ_1 from 119 MPa to 63 MPa might also reduce scatter related to crack initiation from pre-exiting discontinuities. Also, the decrease in σ_z inclines the crack propagation path into surfaces other than normal to specimens' axis, and consequently the constraint against the crack opening increases. Therefore, the specimen is expected to fail under a higher $\tau_{nominal}$ being in fact closer to true value, and also the scatter in test results is expected to decrease. Square flanges will need higher thickness (9 mm) to achieve the same stress distribution (Fig. 6).

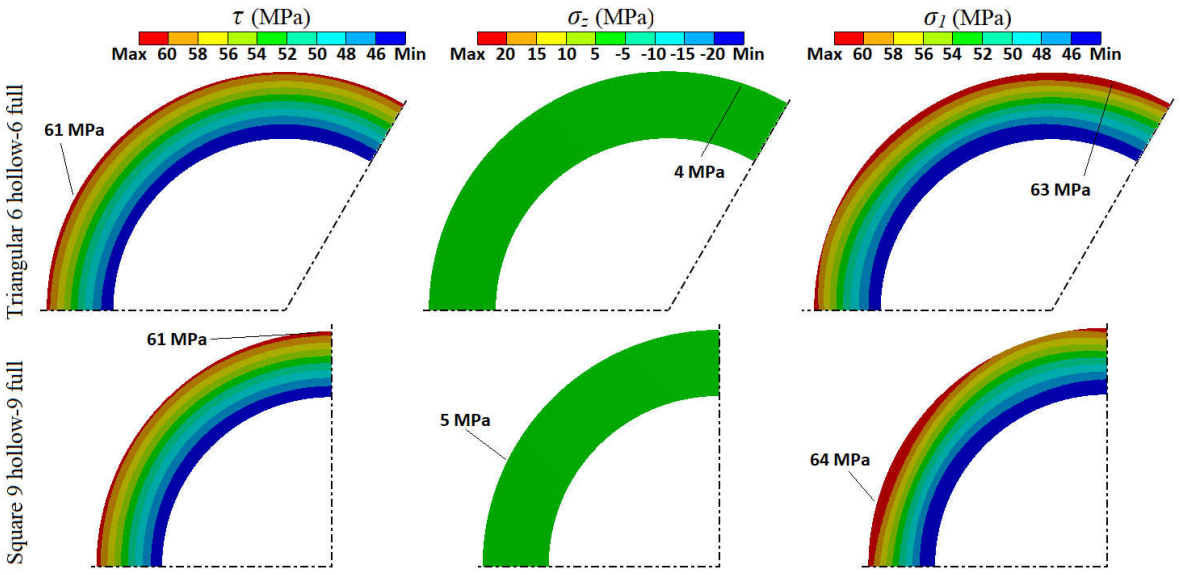

Fig. 6. Distribution of τ, σ_z and σ_1 in the mid-thickness plane of sealant for specimens with 6 mm thick triangular- and 9 mm thick square-flanges at room temperature. The maximum stresses are

indicated along with their respective location. The applied torque corresponds to a nominal shear stress $\tau_{nominal}$ of 60 MPa, which calculated using the analytical relationship.

Figure 7 reveals that the normalized maximum σ_z ($\sigma_{z,max}$ / $\tau_{nominal}$) is almost independent of the applied torque (T), though the normalized maximum shear stress (τ_{max} / $\tau_{nominal}$) value increases with increasing T. This means that a higher torque T causes the shear stress state to deviate more from axial symmetric distribution. Hence, it can be concluded that the difference between nominal and true shear strength increases with increasing the apparent fracture torque (T_f). Therefore, it is important to investigate the stress distributions of the specimens at T_f.

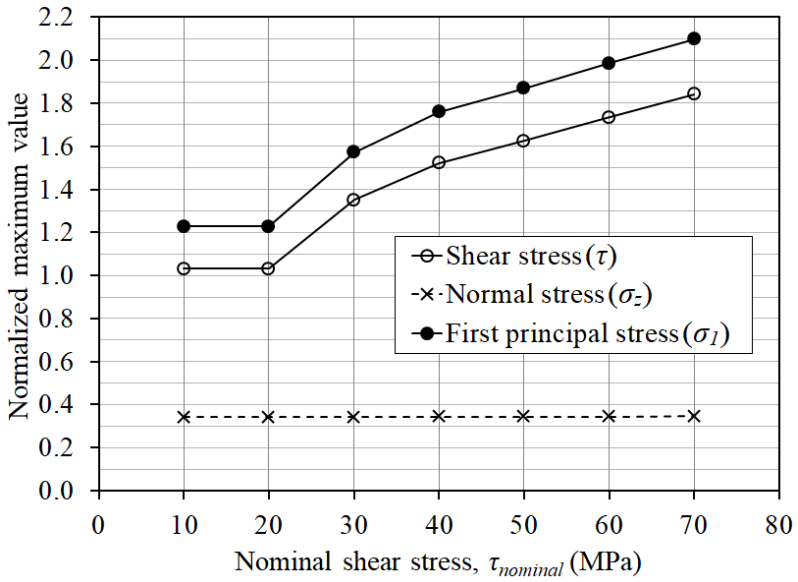

Fig. 7. Normalized maximum stresses in the mid-thickness plane of sealant in 3 hollow-3 full specimen at room temperature as a function of $\tau_{nominal}$.

With increase of the temperature from RT to 600 °C, the elastic moduli of Crofer22APU, Inconel X-750 and sealant G decrease by 33%, 23% and 9% respectively, and, furthermore, the yield strength of the Crofer22APU steel also decreased from 270 MPa to 130 MPa [38–41].

Figure 8 presents the stress distributions in the sealant under a torque corresponding to $\tau_{nominal}$ of 40 MPa at 600 °C. The magnitude of τ and σ_z within the region of stress concentration reach for the square 3 hollow-3 full specimen at 600 °C up to 64 MPa and 14 MPa, respectively. The simulation under the same torque at room temperature yielded the same σ_z distribution but a slightly lower maximum shear stress (61 MPa). Therefore, the temperature change doesn't have a significant effect on the stress distributions, and thus it can be stated that the flanges are not responsible for a lower $\tau_{nominal}$ at 600 °C than at room temperature [20].

Recently, a finite element simulation [16] indicated the presence of a non-negligible thermal residual stress in joined specimens. The impact of thermal residual stresses on $\tau_{nominal}$ decreases with increasing the test temperature (due to decreasing the temperature interval between the joining and testing temperatures). Therefore, it can be stated that the difference in true shear strengths at different temperatures is even greater than in nominal shear strengths. In other words, a lower $\tau_{nominal}$ at higher temperatures originates neither from test uncertainty nor from differences in thermal residual stress, but it is a result of a change in properties of the sealant.

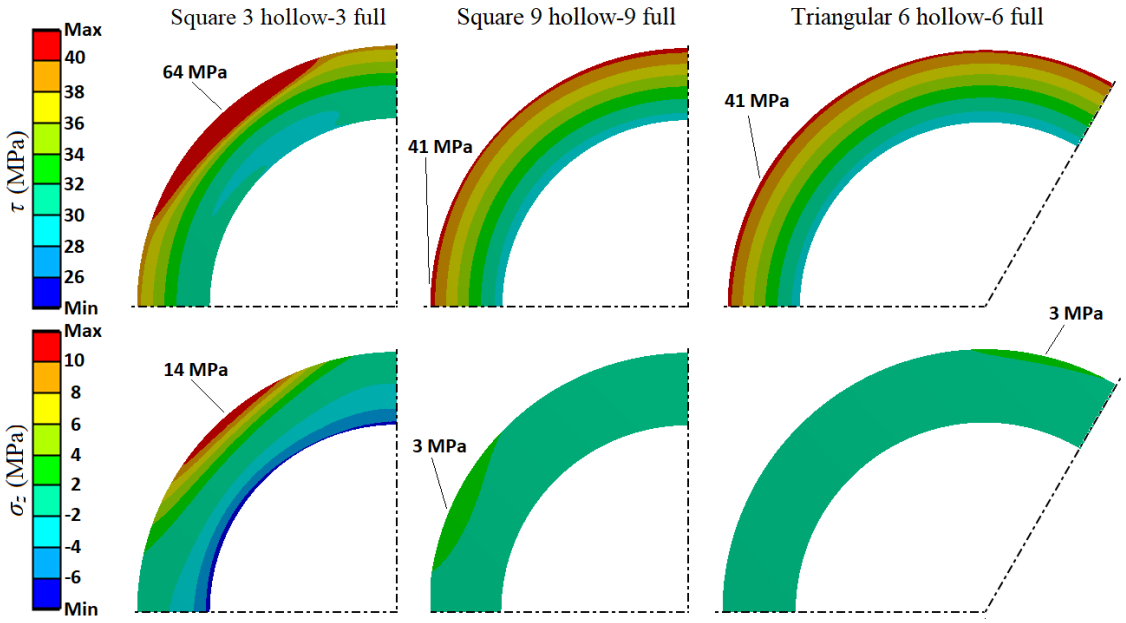

Fig. 8. Distribution of τ and σ_z in the mid-thickness plane of sealant in specimens with 3 mm thick square-, 9 mm thick square- and 6 mm thick triangular-flanges at 600 ºC. The maximum stresses are indicated along with their location. The applied torque corresponds to a nominal shear stress $\tau_{nominal}$ of 40 MPa, which calculated using the analytical relationship.

As seen in Fig. 8, thickening either square or triangular flanges also improves the stress distributions at 600 °C. The stress concentration reduction decreased the plastic strains within the steel halves (near the sealant/steel interface) to almost zero at both temperatures.

The volume of Crofer22APU material used in square 9 hollow-9 full and triangular 9 hollow-9 full specimens is respectively 139 % and 118 % larger than that in the square 3 hollow-3 full specimens. However, these optimized geometries have the potential to bring the measured $\tau_{nominal}$ value closer to the true torsional shear strength and also decrease the scatter in test results.

4. Conclusions

In this study, the stress distributions during torsion testing of glass-ceramic sealant of joint specimens were investigated by finite element method (FEM). The implemented asymmetric model, which simulates conditions closer to reality than previously used models, illustrates the following important points:

- The square flanges (ends) of hourglass-shaped specimens cause the stress state in glass-ceramic sealant to deviate from the axial symmetric pure shear stress distribution. The tensile stress along the specimen axis (σ_z) has the lowest values in the specimen with one full half and annulus-shaped glass-ceramic layer (hollow-full specimen).
- The tensile stress (σ_z) is more detrimental than the first principal stress (σ_1) concentration, because σ_z increases the angle of crack propagation surface to the specimen axis (θ) from 45º to 90 º, where the constraint against the crack opening is lower.
- The change in shape of the flanges from square to triangle slightly reduces σ_z and the shear stress concentrations at the outer edge of glass-ceramic sealant. However, thickening the square and triangular flanges to respectively 9 mm and 6 mm decreases σ_z down to 8% of nominal shear stress and also results in a more symmetric shear stress distribution.
- The measured nominal shear strength ($\tau_{nominal}$) gets closer to the true value if the fracture torque (T_f) is decreased for a given specimens' geometry. This should be taken into consideration in cases where the shear strengths of glass-ceramic/steel joints change with temperature.

- A lower nominal shear strength ($\tau_{nominal}$) of joints at higher temperatures originates neither from test uncertainty nor from differences in thermal residual stresses, but it is associated with the properties of sealants.

Acknowledgements

The authors wish to thank Mr. D. Federmann and Ms. T. Osipova for the support in preparations and testing of reference specimens, Dr. V. Ebrahimzade Isfahani for great help in supporting simulations and Prof. L. Singheiser and Prof. M. Krüger for hosting at Forschungszentrum Jülich. M. Fakouri Hasanabadi, Prof. A.H. Kokabi and Dr. M.A. Faghihi-Sani express their gratitude to Ministry of Science, Research and Technology of Iran, Iran's National Elites Foundation and also the research board of Sharif University of Technology for financial support and providing the research facilities.

References

[1] M. Fakouri Hasanabadi, Investigation of mechanical properties of glass-ceramic sealant for solid oxide fuel/electrolysis cells, Sharif University of Technology, Tehran, Iran, 2018. doi:10.13140/RG.2.2.15805.72161.

[2] I.D. Bloom, K.L. Ley, Compliant sealants for solid oxide fuel cells and other ceramics, US Patent 5453331, 1995.

[3] K.L. Ley, M. Krumpelt, R. Kumar, J.H. Meiser, I. Bloom, Glass-ceramic sealants for solid oxide fuel cells: Part I. Physical properties, J. Mater. Res. 11 (1996) 1489–1493. doi:10.1557/JMR.1996.0185.

[4] Q. Zhu, L. Peng, T. Zhang, Stable Glass Seals for Intermediate Temperature (IT) SOFC Applications, in: Fuel Cell Electron. Packag., Springer US, Boston, MA, 2007: pp. 33–60. doi:10.1007/978-0-387-47324-6_2.

[5] Z. Gao, L. V Mogni, E.C. Miller, J.G. Railsback, S.A. Barnett, A perspective on low-temperature solid oxide fuel cells, Energy Environ. Sci. 9 (2016) 1602–1644. doi:10.1039/C5EE03858H.

[6] N.P. Brandon, E. Ruiz-Trejo, P. Boldrin, Solid Oxide Fuel Cell Lifetime and Reliability, Academic Press, London, UK, 2017.

[7] A. Atkinson, A.J. Marquis, Mechanical stability, in: W. Vielstich, A. Lamm, H.A. Gasteiger (Eds.), Handb. Fuel Cells, John Wiley & Sons, Ltd, Chichester, UK, 2010. doi:10.1002/9780470974001.f500032.

[8] J. Malzbender, R.W. Steinbrech, L. Singheiser, A review of advanced techniques for

characterising SOFC behaviour, Fuel Cells. 9 (2009) 785–793. doi:10.1002/fuce.200800110.
[9] H. Abdoli, P. Alizadeh, D. Boccaccini, K. Agersted, Effects of thermal aging on thermo-mechanical behavior of a glass sealant for solid oxide cell applications, J. Eur. Ceram. Soc. 34 (2014) 2525–2534. doi:10.1016/j.jeurceramsoc.2014.02.004.
[10] L. Blum, L.G.J. de Haart, J. Malzbender, N. Margaritis, N.H. Menzler, Anode-Supported Solid Oxide Fuel Cell Achieves 70 000 Hours of Continuous Operation, Energy Technol. 4 (2016) 939–942. doi:10.1002/ente.201600114.
[11] J. Malzbender, R.W. Steinbrech, L. Singheiser, Determination of the interfacial fracture energies of cathodes and glass ceramic sealants in a planar solid-oxide fuel cell design, J. Mater. Res. 18 (2003) 929–934. doi:10.1557/JMR.2003.0127.
[12] H. Abdoli, P. Alizadeh, D. Boccaccini, H.L. Frandsen, B.F. Sørensen, S. Molin, K. Agersted, Bonding characteristics of glass seal/metallic interconnect for SOFC applications: Comparative study on chemical and mechanical properties of the interface, in: 13th Int. Conf. Eur. Ceram. Soc., Limoges, France, 2013.
[13] I. Ritucci, R. Kiebach, B. Talic, L. Han, P. Zielke, P. V. Hendriksen, H.L. Frandsen, Improving the interface adherence at sealings in solid oxide cell stacks, J. Mater. Res. (2019) 1–12. doi:10.1557/jmr.2018.459.
[14] M. Fakouri Hasanabadi, A.H. Kokabi, A. Nemati, S. Zinatlou Ajabshir, Interactions near the triple-phase boundaries metal/glass/air in planar solid oxide fuel cells, Int. J. Hydrogen Energy. 42 (2017) 5306–5314. doi:10.1016/j.ijhydene.2017.01.065.
[15] S.-F. Wang, H.-C. Lu, Y.-X. Liu, Y.-F. Hsu, Z.-Y. Liu, Characteristics of glass sealants for intermediate-temperature solid oxide fuel cell applications, Ceram. Int. 43 (2017) S613–S620. doi:10.1016/j.ceramint.2017.05.211.
[16] M. Fakouri Hasanabadi, M.A. Faghihi-Sani, A.H. Kokabi, S.M. Groß-Barsnick, J. Malzbender, Room- and high-temperature flexural strength of a stable solid oxide fuel/electrolysis cell sealing material, Ceram. Int. 45 (2019) 733–739. doi:10.1016/j.ceramint.2018.09.236.
[17] Y. Zhao, J. Malzbender, Elevated temperature effects on the mechanical properties of solid oxide fuel cell sealing materials, J. Power Sources. 239 (2013) 500–504. doi:10.1016/j.jpowsour.2013.04.043.
[18] C.K. Lin, T.W. Lin, S.H. Wu, W.H. Shiu, C.K. Liu, R.Y. Lee, Creep rupture of the joint between a glass-ceramic sealant and lanthanum strontium manganite-coated ferritic stainless steel interconnect for solid oxide fuel cells, J. Eur. Ceram. Soc. 38 (2018) 2417–2429. doi:10.1016/j.jeurceramsoc.2018.01.016.
[19] B. Ghorbani, K. Vijayaraghavan, A review study on software-based modeling of hydrogen-fueled solid oxide fuel cells, Int. J. Hydrogen Energy. (2019). doi:10.1016/j.ijhydene.2019.03.217.
[20] M. Fakouri Hasanabadi, A.H. Kokabi, M.A. Faghihi-Sani, S.M. Groß-Barsnick, J. Malzbender, Room- and high-temperature torsional shear strength of solid oxide fuel/electrolysis cell sealing material, Ceram. Int. 45 (2019) 2219–2225. doi:10.1016/j.ceramint.2018.10.134.
[21] J. Malzbender, J. Mönch, R.W. Steinbrech, T. Koppitz, S.M. Gross, J. Remmel, Symmetric shear test of glass-ceramic sealants at SOFC operation temperature, J. Mater. Sci. 42 (2007) 6297–6301. doi:10.1007/s10853-006-1178-1.
[22] K.A. Nielsen, M. Solvang, S.B.L. Nielsen, D. Beeaff, Mechanical Behaviour of Glassy Composite Seals for IT-SOFC Application, in: J. Ceram. Eng. Sci., 2008: pp. 315–323.

doi:10.1002/9780470291337.ch31.
[23] C. Lin, J. Chen, J. Tian, L. Chiang, S. Wu, Joint strength of a solid oxide fuel cell glass – ceramic sealant with metallic interconnect, J. Power Sources. 205 (2012) 307–317. doi:10.1016/j.jpowsour.2012.01.048.
[24] H. Javed, A. Sabato, I. Dlouhy, M. Halasova, E. Bernardo, M. Salvo, K. Herbrig, C. Walter, F. Smeacetto, Shear Performance at Room and High Temperatures of Glass–Ceramic Sealants for Solid Oxide Electrolysis Cell Technology, Materials (Basel). 12 (2019) 298. doi:10.3390/ma12020298.
[25] A. Ventrella, M. Salvo, M. Avalle, M. Ferraris, Comparison of shear strength tests on AV119 epoxy-joined ceramics, J. Mater. Sci. 45 (2010) 4401–4405. doi:10.1007/s10853-010-4417-4.
[26] A. Selçuk, A. Atkinson, Measurement of Mechanical Strength of Glass-to-Metal Joints, Fuel Cells. 15 (2015) 595–603. doi:10.1002/fuce.201500028.
[27] C. Shih, Y. Katoh, J.O. Kiggans, T. Koyanagi, H.E. Khalifa, C.A. Back, T. Hinoki, M. Ferraris, Comparison of Shear Strength of Ceramic Joints Determined by Various Test Methods with Small Specimens, in: H.-T. Lin, Y. Katoh, J. Matyáš (Eds.), Ceram. Mater. Energy Appl. IV, John Wiley & Sons, 2015: pp. 139–149. doi:10.1002/9781119040323.ch13.
[28] E.V. V Stephens, J.S.S. Vetrano, B.J.J. Koeppel, Y. Chou, X. Sun, M.A.A. Khaleel, Experimental characterization of glass–ceramic seal properties and their constitutive implementation in solid oxide fuel cell stack models, J. Power Sources. 193 (2009) 625–631. doi:10.1016/j.jpowsour.2009.02.080.
[29] F. Smeacetto, A. De Miranda, A. Ventrella, M. Salvo, M. Ferraris, Shear strength tests of glass ceramic sealant for solid oxide fuel cells applications, Adv. Appl. Ceram. 114 (2015) S70–S75. doi:10.1179/1743676115Y.0000000042.
[30] T. Osipova, J. Wei, G. Pećanac, J. Malzbender, Room and elevated temperature shear strength of sealants for solid oxide fuel cells, Ceram. Int. 42 (2016) 12932–12936. doi:10.1016/j.ceramint.2016.05.064.
[31] B. Cela Greven, S. Gross-Barsnick, T. Koppitz, R. Conradt, F. Smeacetto, A. Ventrella, M. Ferraris, Torsional shear strength of novel glass-ceramic composite sealants for solid oxide fuel cell stacks, Int. J. Appl. Ceram. Technol. 15 (2018) 286–295. doi:10.1111/ijac.12819.
[32] C.H. Henager, B.N. Nguyen, R.J. Kurtz, T.J. Roosendaal, B.A. Borlaug, M. Ferraris, A. Ventrella, Y. Katoh, Modeling and testing miniature torsion specimens for SiC joining development studies for fusion, J. Nucl. Mater. 466 (2015) 253–268. doi:10.1016/j.jnucmat.2015.07.044.
[33] L. Goglio, M. Ferraris, Bonding of ceramics: An analysis of the torsion hourglass specimen, Int. J. Adhes. Adhes. 70 (2016) 46–52. doi:10.1016/j.ijadhadh.2016.05.006.
[34] M. Fakouri Hasanabadi, M.A. Faghihi-Sani, A.H. Kokabi, J. Malzbender, The analysis of torsional shear strength test of sealants for solid oxide fuel cells, Ceram. Int. 43 (2017) 12546–12550. doi:10.1016/j.ceramint.2017.06.128.
[35] J. Brendt, S.M. Gross-Barsnick, C. Babelot, G. Natour, Nucleation and crystallization processes of glass- ceramic sealants for SOFCs, in: N. Brandon, A. Bertei, P. Boldrin, R. Dawson, K. Kareh, J.-S. Kim, Z. Kurban, M. Matian, P. Shearing, F. Tariq, E.R. Trejo, V. Yufit (Eds.), 2th Eur. SOFC SOE Forum, European Fuel Cell Forum AG, Lucerne, Switzerland, 2016: pp. 73–82.
[36] S.-M. Groß, U. Reisgen, Glaslöten - eine anspruchsvolle Fügetechnik nicht nur für die Hochtemperatur-Brennstoffzelle, Schweißen Und Schneid. 59 (2007) 70–7. http://juser.fz-

juelich.de/record/56112.
[37] B. Cela, S. Sillapawatana, S. M. Gross, T. Koppitz, R. Conradt, Influence of Filler Additives on the Effective Viscosity of Glass-Ceramic Composite Sealants, J. Univ. Chem. Technol. Metall. 47 (2012) 449–458. http://dl.uctm.edu/journal/node/j2012-4/14_Beatriz Cela_449-458.pdf.
[38] J. Malzbender, Y. Zhao, Flexural strength and viscosity of glass ceramic sealants for solid oxide fuel cell stacks, Fuel Cells. 12 (2012) 47–53. doi:10.1002/fuce.201100116.
[39] Crofer 22 APU Material data sheet No. 4046, ThyssenKrupp VDM, Germany, May, 2010. https://www.vdm-metals.com/fileadmin/user_upload/Downloads/Data_Sheets/Data_Sheet_VDM_Crofer_22_APU.pdf.
[40] T.T. Molla, F. Greco, K. Kwok, P. Zielke, H.L. Frandsen, Development of High Temperature Mechanical Rig for Characterizing the Viscoplastic Properties of Alloys Used in Solid Oxide Cells, J. Test. Eval. 46 (2018) 20170046. doi:10.1520/JTE20170046.
[41] Inconel X-750 technical data, High Temp Metals, California, USA, 2018. http://www.hightempmetals.com/techdata/hitempInconelX750data.php.
[42] ASTM F734 − 17, Standard Test Method for Shear Strength of Fusion Bonded Polycarbonate Aerospace Glazing Material, (2017). doi:10.1520/F0734-95R11.2.
[43] Y.-I. Jung, J.-H.J.-Y. Park, H.-G. Kim, D.-J. Park, J.-H.J.-Y. Park, W.-J. Kim, Effect of Ti and Si Interlayer Materials on the Joining of SiC Ceramics, Nucl. Eng. Technol. 48 (2016) 1009–1014. doi:10.1016/j.net.2016.03.001.
[44] J.W. Hutchinson, Z. Suo, Mixed mode cracking in layered materials, in: Adv. Appl. Mech., 1991: pp. 63–191. doi:10.1016/S0065-2156(08)70164-9.
[45] F.P. Beer, J. E. Russell Johnston, J.T. Dewolf, D.F. Mazurek, Mechanics of Materials, 6th ed., McGraw-Hill, New York, NY, USA, 2012.
[46] J. Wei, Mechanical Characterization of Solid Oxide Fuel Cells and Sealants, RWTH Aachen, Aachen, Germany, 2016. doi:10.18154/RWTH-2017-04301.